nature physics

Article

https://doi.org/10.1038/s41567-023-02316-9

Edge supercurrent reveals competition between condensates in a Weyl superconductor

Received: 7 September 2022

Stephan Kim • 1,2, Shiming Lei³, Leslie M. Schoop • 3, R. J. Cava³ & N. P. Ong • 1

Accepted: 3 November 2023

Published online: 11 January 2024

Check for updates

In topological materials, the edge states are readily distinguished from the bulk states. The situation where a topological semimetal becomes superconducting so that Cooper pairs occupy both the bulk and the edge states is not well understood. In particular, we do not know if we can force their pairing symmetries to be different. Here we show that, when supercurrent is injected into the superconducting Weyl semimetal MoTe₂ from Nb contacts, the invasive s-wave pairing potential from Nb is incompatible with the intrinsic Cooper pair condensate in MoTe₂. This incompatibility leads to strong stochasticity in the switching current and an unusual anti-hysteretic behaviour in the current-voltage loops. There is also an asymmetry in the edge oscillations where, as the magnetic field crosses zero, the phase noise switches from one with a noisy spectrum to one that is noise free. Using the noise spectrum as a guide, we track the anomalous features to field-induced switching of the device gap function between s-wave symmetry and the unconventional symmetry intrinsic to MoTe₂. We infer that the behaviour of the gap function along the edges is different from that in the bulk.

In the subfield of topological superconductivity, a key issue is the observation and manipulation of an edge supercurrent that flows on the boundaries of a sample $^{1-4}$. In the T_d phase of MoTe₂, bulk superconductivity appears at 100 mK. Evidence for an edge supercurrent was recently derived from rapid oscillations of the critical current I_c induced by fluxoid quantization⁵. As the magnetic field *H* is slowly increased, fluxoid quantization leads to a sawtooth field profile for the edge superfluid velocity \mathbf{v}_{s} , which translates to oscillations of I_c observable in a colour map plot of the differential resistance dV/dI versus H (where a fluxoid is a flux quantum ϕ_0 plus the superfluid circulation; Supplementary Section VI). In this Article, when supercurrent is injected from niobium contacts, we observe a host of anomalous features driven by incompatibility between pairing with s-wave symmetry and the symmetry intrinsic to MoTe₂. The features also reflect the field-induced switching of the device gap function between the two pairing symmetries. By varying the contact geometry across eight devices, we can distinguish edge state features from those in the bulk.

Because the interfaces between Nb and MoTe₂ have high transmittivity at 20 mK, our experiment lies in the strong-coupling proximity effect regime, well beyond the Josephson effect regime (Supplementary Section V). In strong-coupling junctions, the system (Nb plus MoTe₂) is treated as a single superconductor with a unique critical temperature T_c and a gap function $\hat{\Psi}(\mathbf{r})$ that is inhomogeneous (\mathbf{r} is the spatial coordinate in the device)⁶⁻¹¹. In device SA, the T_c of approximately 850 mK lies well above the unperturbed T_c of pristine MoTe₂ (100 mK) but still far below that of Nb (approximately 8 K). Similarly, the critical field and peak critical current are greatly enhanced over the values in pristine MoTe₂.

To discuss the proximity effect (Supplementary Section VII)⁶⁻¹¹, we denote the Gor'kov pair amplitude in Nb by $\eta(\mathbf{r}) = \langle \hat{\psi}_{\downarrow}(\mathbf{r})\hat{\psi}_{\uparrow}(\mathbf{r}) \rangle$, where $\hat{\psi}_{\alpha}(\mathbf{r})$ annihilates an electron in spin state $\alpha = \uparrow$, \downarrow at \mathbf{r} . We call

¹Departments of Physics, Princeton University, Princeton, NJ, USA. ²Department of Electrical and Computer Engineering, Princeton University, Princeton, NJ, USA. ³Department of Chemistry, Princeton University, Princeton, NJ, USA. ³Department of Chemistry, Princeton University, Princeton, NJ, USA. ³Department of Chemistry, Princeton University, Princeton, NJ, USA. ⁴Department of Chemistry, Princeton University, Princeton, NJ, USA. ⁵Department of Chemistry, Princeton University, Princeton, NJ, USA. ⁵Department of Chemistry, Princeton University, Princeton, NJ, USA. ⁵Department of Chemistry, Princeton University, Princeton, NJ, USA. ⁶Department of Chemistry, Princeton University, Princeton, NJ, USA. ⁷Department of Chemistry, Princeton University, Princeton, NJ, USA. ⁸Department of Chemistry, Princeton University, Princeton, NJ, USA. ⁹Department of Chemistry, Princeton, Pri

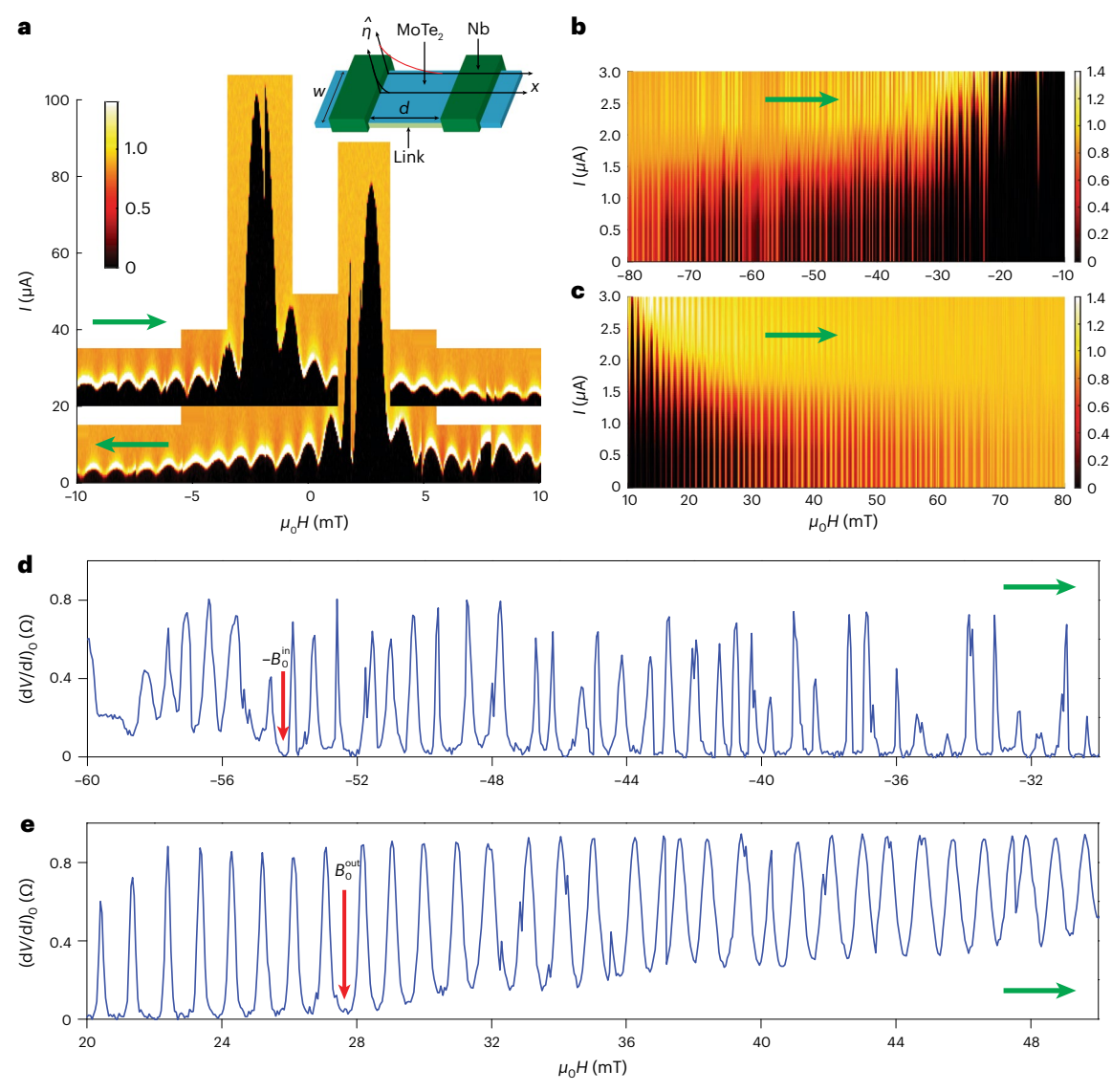


Fig. 1| Anti-hysteretic central peak and edge oscillations observed in MoTe₂ measured by supercurrent injection from Nb pads in device SA at 18 mK. a, Colour map of the differential resistance dV/dI plotted versus magnetic field H and current I. Dissipationless regions are shown in black (colour scale at left). The central peak occurs at -3 or +3 mT when H is scanned from left to right or right to left, respectively. The inset defines the width w and spacing d of the device. The decays of the Nb pairing amplitude η in the bulk (black curve) and

along an edge (red) are sketched. **b,c**, Fluxoid-induced edge oscillations on the inbound $(\mathbf{d}|H|/dt < 0, \mathbf{a})$ and outbound branches $(\mathbf{d}|H|/dt > 0, \mathbf{b})$. **d,e**, The zero-bias differential resistance $(\mathbf{d}V/dl)_0$ versus H on the inbound (\mathbf{d}) and outbound branches (\mathbf{e}) . The phase noise is much larger in \mathbf{d} than in \mathbf{e} . The transition to dissipationless behaviour $((\mathbf{d}V/dl)_0 \rightarrow 0)$ occurs at $-B_0^{\text{in}} = -54$ mT and $B_0^{\text{out}} = +28$ mT in \mathbf{d} and \mathbf{e} , respectively (red arrows). The green arrow in $\mathbf{b}-\mathbf{e}$ indicates the field scan direction.

the pair amplitude in pristine MoTe₂ (of unknown symmetry) $F_{\alpha\beta}(\mathbf{r}) = \langle \hat{\psi}_{\alpha}(\mathbf{r}) \hat{\psi}_{\beta}(\mathbf{r}) \rangle$. A key inference is that cycling of H causes $\hat{\Psi}(\mathbf{r})$ to switch between s-wave symmetry and $F_{\alpha\beta}$ symmetry. Aside from MoTe₂, evidence for edge supercurrents has also been reported in bismuth nanowires¹² and in a kagome superconductor¹³.

Anti-hysteretic behaviour of the central peak

Figure 1a shows a colour map of the differential resistance dV/dI versus H and the current I measured in device SA at a temperature T of 18 mK. At weak H, supercurrent injection from Nb leads to a large critical current I_c within a narrow central peak (shaded black) that reaches peak values of approximately 80 μ A (20 times larger than seen in pristine crystals). The central peak is observed in an anomalous position in H. In conventional superconductors, we expect H to cross zero before the flux density B does. Instead, the central peak here emerges before H reaches zero for either scan (which seems oddly anti-causal). We dub this curious pattern anti-hysteretic.

When $|\mu_0 H|$ exceeds 10 mT, we observe a dense array of periodic peaks in the colour map (Fig. 1b,c). These are the fluxoid-induced oscillations⁵, now persisting to 90 mT (compared with 3 mT in pristine crystals). As shown in Fig. 1d,e, the oscillations appear as narrow peaks in the differential resistance $(dV/dI)_0$ measured at I=0. At each peak, \mathbf{v}_s reverses direction to admit a fluxoid⁵.

$Stochastic\,switching$

Incompatibility between s-wave pairing induced by Nb and $F_{\alpha\beta}$ is most evident in I-V curves measured when H lies within the central peak in Fig. 1a. The switching transition is strongly stochastic (Supplementary Section II). Figure 2a shows 100 curves of dV/dI versus I measured at 18 mK in device SC with μ_0H fixed at -2.5 mT. The critical currents $\{I_c\}$ obey a distribution function $P(I_c, H)$ that is distinctly bimodal, with a histogram that shows a major peak at $10.5~\mu A$ and a minor one at $8.5~\mu A$ (Fig. 2b and Supplementary Section II). In the colour map of dV/dI(H, I) (Fig. 1a), the stochastic nature of the distribution is also apparent as

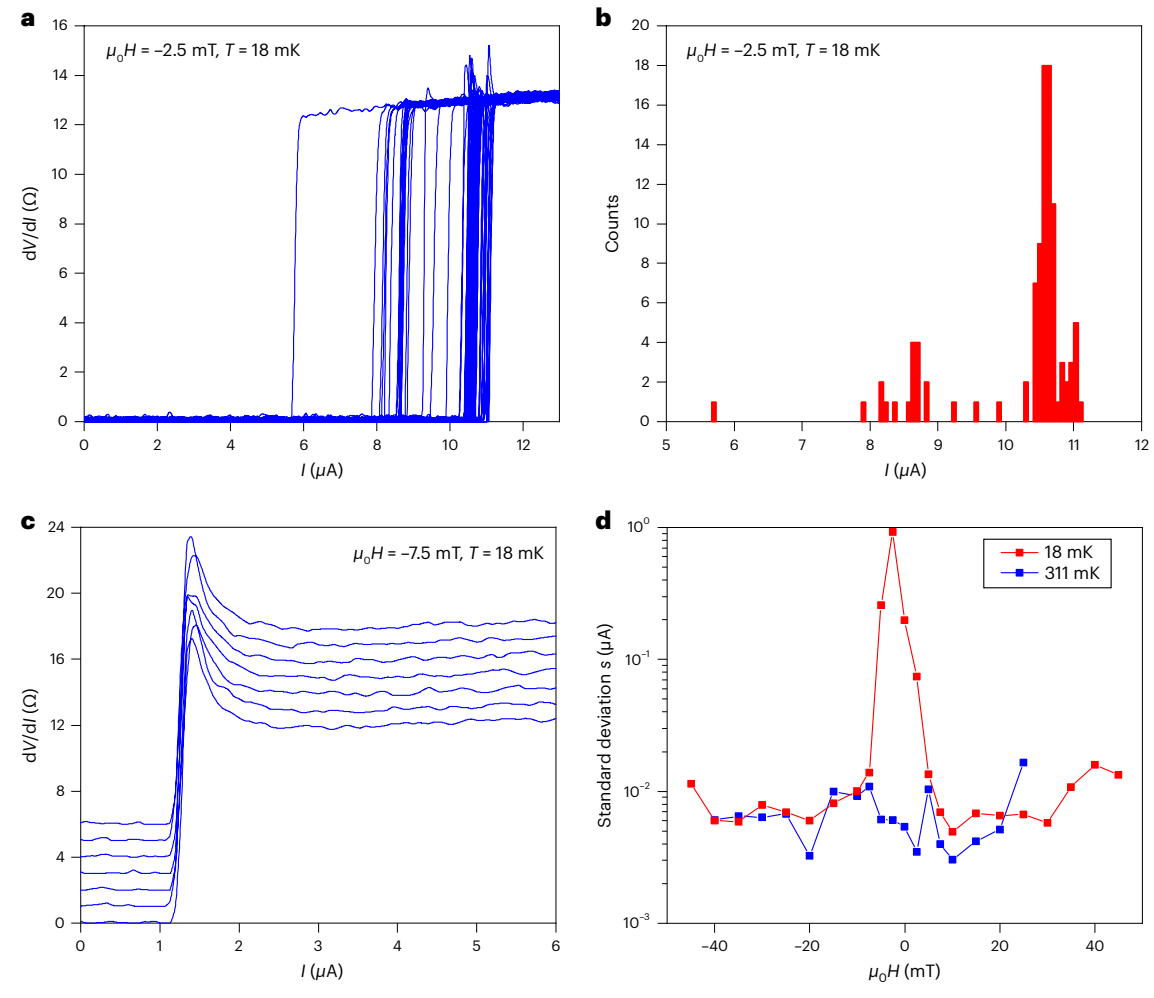


Fig. 2 | **Stochastic switching in bulk states measured in device SC. a**, The critical current in 100 curves of dV/dI versus I, showing bunching of I_c suggestive of a bimodal distribution $P(I_c, H)$. When H lies within the central peak $(\mu_0 H = -2.5 \text{ mT})$, the switch from dissipationless to dissipative behaviour is stochastic. **b**, A histogram plot of $P(I_c, H)$, confirming the bimodal distribution.

However, when H lies outside the central peak ($-7.5\,\mathrm{mT}$), the switching transitions are non-stochastic. In all 100 scans, the transition occurs at $1.27\pm0.01\,\mu\mathrm{A}$. **c**, Seven of the scans measured at $-7.5\,\mathrm{mT}$. **d**, The standard deviation s versus H of the distribution $P(I_c, H)$ at $18\,\mathrm{mK}$ (Supplementary Section II). At the peak, s is $100\,\mathrm{fold}$ larger than its value outside the peak. At $311\,\mathrm{mK}$, the peak is unresolved.

random spikes within the central peak. By contrast, outside the central peak ($\mu_0 H = -7.5 \text{ mT}$), the distribution $P(I_c, H)$ becomes very narrow (Fig. 2c). The standard deviation s(H) (Fig. 2d; obtained from 100 scans at each H) provides a measure of the stochasticity. The profile s(H) displays a narrow peak at the central peak with peak value 100 fold larger than the baseline (red curve). At 311 mK, however, the peak is absent (blue curve).

Phase noise and anti-hysteretic $(dV/dI)_0$ curves

The competition between $F_{\alpha\beta}$ and the Nb pair amplitude η also has a strong effect on the phase noise of the oscillations in $(dV/dI)_0$. We call field scans 'inbound' if |H| decreases with time and 'outbound' if |H| increases. On inbound branches (Fig. 1b,d), the noise content of the oscillations is invariably very large, whereas on outbound branches (Fig. 1c,e), it is suppressed, especially in the interval $5 < \mu_0 H < 45$ mT, which we call the 'quiet zone'.

Figure 3 emphasizes the asymmetry by showing the colour map of the oscillations over the entire field range. On the inbound branch (Fig. 3a), the noise content is much higher than on the outbound branch (Fig. 3d). To quantify the phase noise, we express the fluctuations in the frequency as an H-dependent phase $\theta(H)$ (Supplementary Section III). It is expedient to subtract from $\theta(H)$ a background $\theta_0(H)$ derived from an H-linear fit to $\theta(H)$ in the quiet zone (5, 45) mT

(Supplementary Section III). The deviation $\Delta\theta(H)=\theta(H)-\theta_0(H)$ then highlights field intervals with large phase noise. In Fig. 3b, $\Delta\theta$ on the inbound branch (blue curve) is seen to be much larger than that on the outbound curve (red). In the quiet zone (5, 45) mT, $\Delta\theta$ is flat by design. We also employ the smoothed derivative $\langle \mathrm{d}\Delta\theta/\mathrm{d}\mu_0H\rangle$, which is more sensitive to local changes in frequency. As seen in Fig. 3c, $\langle \mathrm{d}\Delta\theta/\mathrm{d}\mu_0H\rangle$ is much larger on the inbound branch than in the quiet zone on the outbound branch.

Aside from the oscillations, $(dV/dI)_0$ also displays a dissipationless regime bracketed by the two fields $B_0^{\rm in}$ and $B_0^{\rm out}$ (Fig. 1d,e, red arrows). An expanded view of these transitions is shown in Fig. 4a–h for four devices. In device SA, the transition on the inbound branch occurs at $-B_0^{\rm in}=-54$ mT, larger in magnitude than the field ($B_0^{\rm out}=28$ mT) on the outbound branch (Fig. 4e, blue curves). The reverse sweep (red curves) is the mirror reflection of the blue curve. The curves are again anti-hysteretic.

Distinguishing edge from bulk supercurrents

The observed supercurrents segregate into two groups. In group I (Fig. 1a, central peak), the peak I_c is very large (80 μ A) but is easily suppressed at weak μ_0H (3–5 mT). The second group (II) are the weak supercurrents (1–2 μ A) seen in the oscillations in (dV/dI) $_0$ which survive to fields up to 90 mT (Figs. 1 and 3).

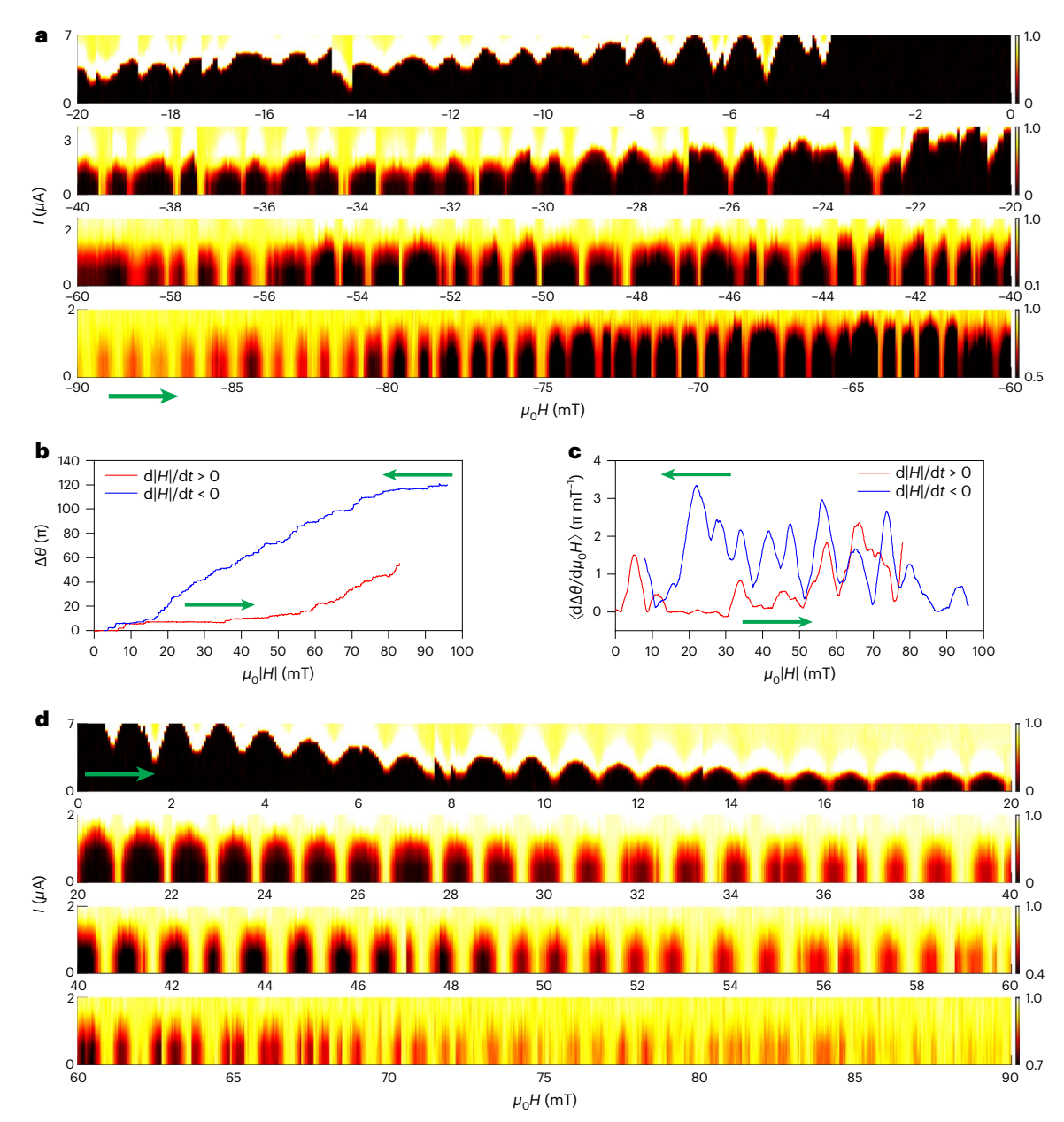


Fig. 3 | **Nature of the phase noise in the fluxoid-induced oscillations over the full field interval in sample SA at 18 mK. a**, Four strips showing the observed colour map of dV/dI in the H-I plane as H is scanned from -90 mT to 0 mT (inbound branch). Initially $(-90 < \mu_0 H < -80$ mT), the phase noise is quite small. Between -80 mT and -12 mT, the emergence of large phase noise strongly distorts the oscillations. The noise is dominated by 2π jumps in the phase $\theta(H)$ that lead to random compressions and dilations of the period. We attribute the noise to incompatibility between edge pairing induced by η (Nb) and the intrinsic pair amplitude $F_{\alpha\beta}$ in the vortex-liquid state of MoTe₂. **b**, A comparison of the curves of the phase deviation $\Delta\theta(H)$ in the inbound branch (blue) with

the outbound branch (red). $\Delta\theta(H)=\theta(H)-\theta_0(H)$ measures the phase deviation caused by random phase jumps accumulated over the entire field interval (see text). ${\bf c}$, A comparison of the smoothed derivative $\langle {\rm d} \Delta\theta/{\rm d} \mu_0 H \rangle$ between the inbound (blue) and outbound branches (red). The large phase noise in the inbound branch causes $\langle {\rm d} \Delta\theta/{\rm d} \mu_0 H \rangle$ to lie well above that for the outbound branch, especially between 5 and 45 mT. ${\bf d}$, Four strips showing the colour map of ${\rm d} V/{\rm d} I$ as $\mu_0 H$ is swept from 0 to 90 mT (outbound branch). Over the quiet zone (5–45 mT), the phase noise is negligible except for isolated 2π jumps (at 13.4, 35 and 36.5 mT). The green arrows in ${\bf b}$ and ${\bf c}$ indicate the field scan direction.

By tailoring the contact designs in eight devices, we found that the group II features are specific to edge states. The oscillation period corresponds to a fluxoid area \mathcal{A}_{ϕ} bracketed by the Nb contacts (Supplementary Section I). Its perimeter comprises two segments (of length w) lying under Nb contacts plus two segments called links (of length ℓ_1 and ℓ_2) at the uncovered physical edges (Fig. 1a, inset).

In five devices (SA, SK, SI, SJ and SB) the Nb contacts are laid down as parallel strips with spacing *d* (Fig. 4 and Supplementary Table S1 and Fig. S3). In the remaining three devices (SF, SH and SD),

the Nb contacts are progressively reduced in volume while ℓ_1 and ℓ_2 are greatly lengthened. These changes strongly attenuate group II features.

Figure 4 shows two parallel-strip devices (SA and SI, Fig. 4a and 4b, respectively) and two devices (SH and SD) in the second series (Fig. 4c and 4d, respectively). The corresponding $(dV/dI)_0$ curves are displayed in Fig. 4e-h, together with the colour maps in Fig. 4i-j. Group II features are prominently seen in devices SA and SI where we have $2w \gg \ell_1 = \ell_2 = d$. As we increase d, the widths of the anti-hysteretic loops decrease.

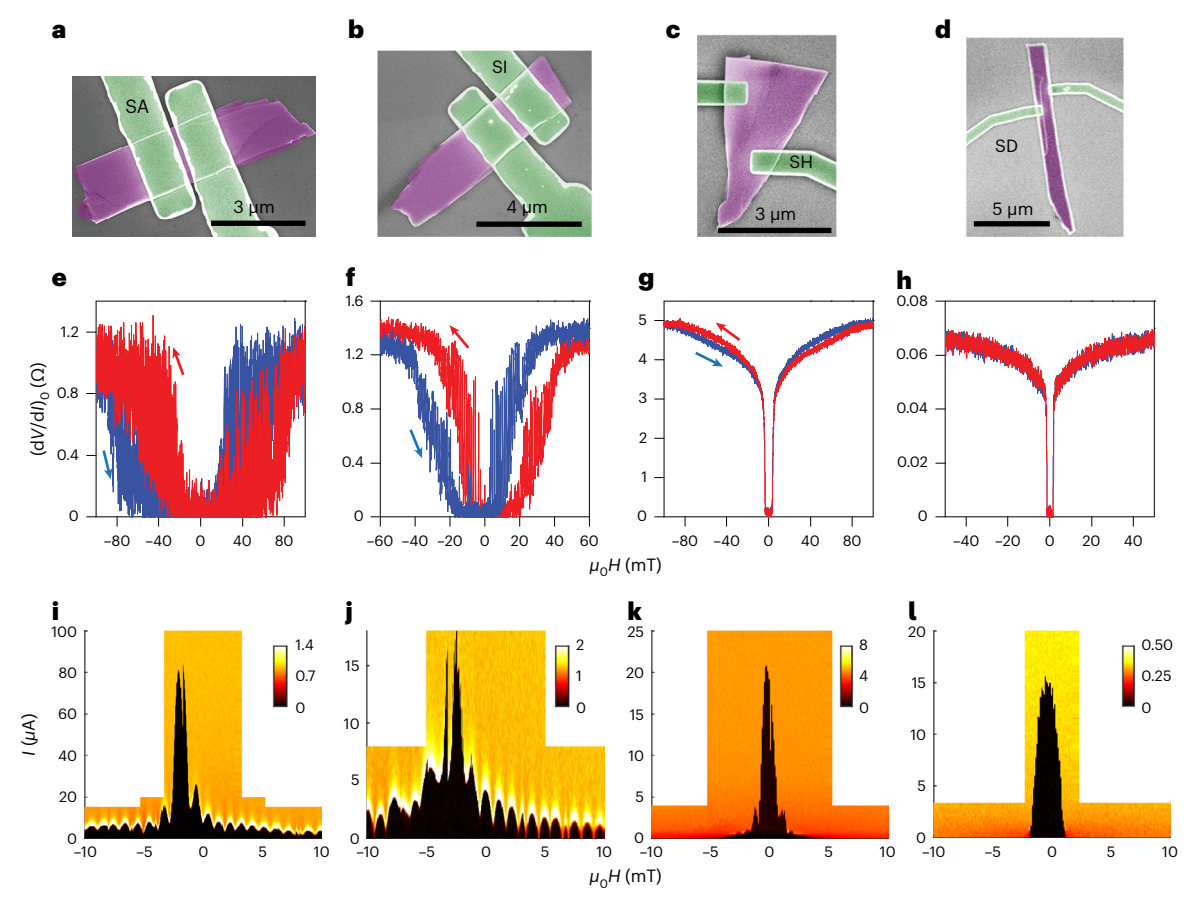


Fig. 4 | **Systematic suppression of edge oscillations and anti-hysteresis in four devices. a–d,** Device SA (**a**), SI (**b**), SH (**c**) and SD (**d**). Devices SA and SI (with spacing d of 156 and 285 nm, respectively) are examples from a series of five parallel-strip devices. Devices SH and SD are from a second series in which the Nb contact volumes are decreased while ℓ_1 and ℓ_2 are progressively increased. **e–h**, Anti-hystereses in (dV/dI)₀ versus H (blue and red arrows indicate field scan directions) for device SA (**e**), SI (**f**), SH (**g**) and SD (**h**). **i–l**, Colour maps of

 $dV/dI versus \textit{H} \ and \textit{I} \ for \ device \ SA\ (\textbf{i)}, SI\ (\textbf{j)}, SH\ (\textbf{k}) \ and \ SD\ (\textbf{l)}. \ In \ devices \ SA\ and \ SI, prominent anti-hysteresis and edge oscillations are seen, in both <math>(dV/dI)_0$ (e and f) and their colour maps (i and j). In devices SH and SD, these group II features are suppressed or absent in $(dV/dI)_0$ (g and h) and in the colour maps (k and I). Supplementary Table S1 presents the parameters for the eight devices, and Supplementary Fig. S3 shows the results for devices SK, SJ, SB and SF.

In devices SH (with ℓ_1 = 5,420 and ℓ_2 = 5,710 nm) and SD (ℓ_1 = 8,030 nm and ℓ_2 = 17,670 nm), the edge oscillations and anti-hystereses are completely suppressed (aside from residual wings in SH). Data from four other samples are shown in Supplementary Fig. S3.

In devices SA and SI, supercurrent in the bulk flows in parallel with supercurrent in the links if |H| is weak. When $|\mu_0H|$ exceeds approximately 4 mT, the bulk supercurrent is suppressed but the link supercurrents survive to large H because they are one dimensional. This robustness enables fluxoid oscillations to be observed up to 90 mT. From measurements on the eight devices, we infer a length scale of $\lambda \approx 800$ nm that measures the effective coherence length of the Nb pairing potential along a link. Group II features are prominent if $\ell_1, \ell_2 < \lambda$ (Fig. 4e,f), whereas they vanish if $\ell_1, \ell_2 > \lambda$ (Fig. 4g,h). We infer that the Nb pairing potential extends quite a long distance along the links compared with the bulk (800 nm versus 40 nm) and also survives to much larger H (Fig. 1a, inset, red and black curves). These findings establish that the group II features arise from edge supercurrents at the links.

By comparison, the much larger peak I_c values of the group I supercurrents (Fig. 1a, central peak) suggest a bulk origin. The 20-fold decrease in the peak I_c value as d increases from 156 to 703 nm also implies bulk states with s-wave symmetry (Supplementary Table S1). The decrease is consistent with the short coherence length of Nb in the bulk ($\xi_0 \approx 40$ nm).

Proximity effect between competing symmetries

In de Gennes' treatment of the proximity effect (valid in the small-gap regime), the amplitude for a Cooper pair to propagate between points \mathbf{r}' and \mathbf{r} is given by the kernel $K(\mathbf{r}, \mathbf{r}')$ (refs. 6,8,11) (Supplementary Section VII). Whenever a propagator segment lies in Nb, $K(\mathbf{r}, \mathbf{r}')$ gains a large enhancement from the strong s-channel attraction. Hence, the gap function $\hat{\Psi}(\mathbf{r})$ in MoTe₂ adopts either the $F_{\alpha\beta}$ symmetry or s-wave symmetry as dictated by the sum over propagators going from all points \mathbf{r}' to \mathbf{r} . Within either superconductor, the sum reflects the amplitude in the favoured pairing channel and the volume (Supplementary Equation (S23)). An applied field H can tip the balance by selectively weakening one or the other condensation amplitude. Calculations beyond the linear-gap regime show how the gap function changes symmetry in a junction between an s- and a p-wave superconductor.

At H=0 in our devices, the weighted sum favours $F_{\alpha\beta}$. Vortices inserted by H initially form a vortex solid whose long-range phase coherence preserves the stability of the $F_{\alpha\beta}$ state throughout the bulk. As |H| increases, melting of the vortex solid destroys long-range phase coherence, which weakens the pair amplitude $F_{\alpha\beta}$. This tilts the balance to s-wave symmetry in $\hat{\Psi}$ until |H| becomes large enough to suppress the s-wave condensate in the bulk. At large |H|, $\hat{\Psi}$ reverts to the $F_{\alpha\beta}$ symmetry in the vortex liquid state, which survives to 80 mT

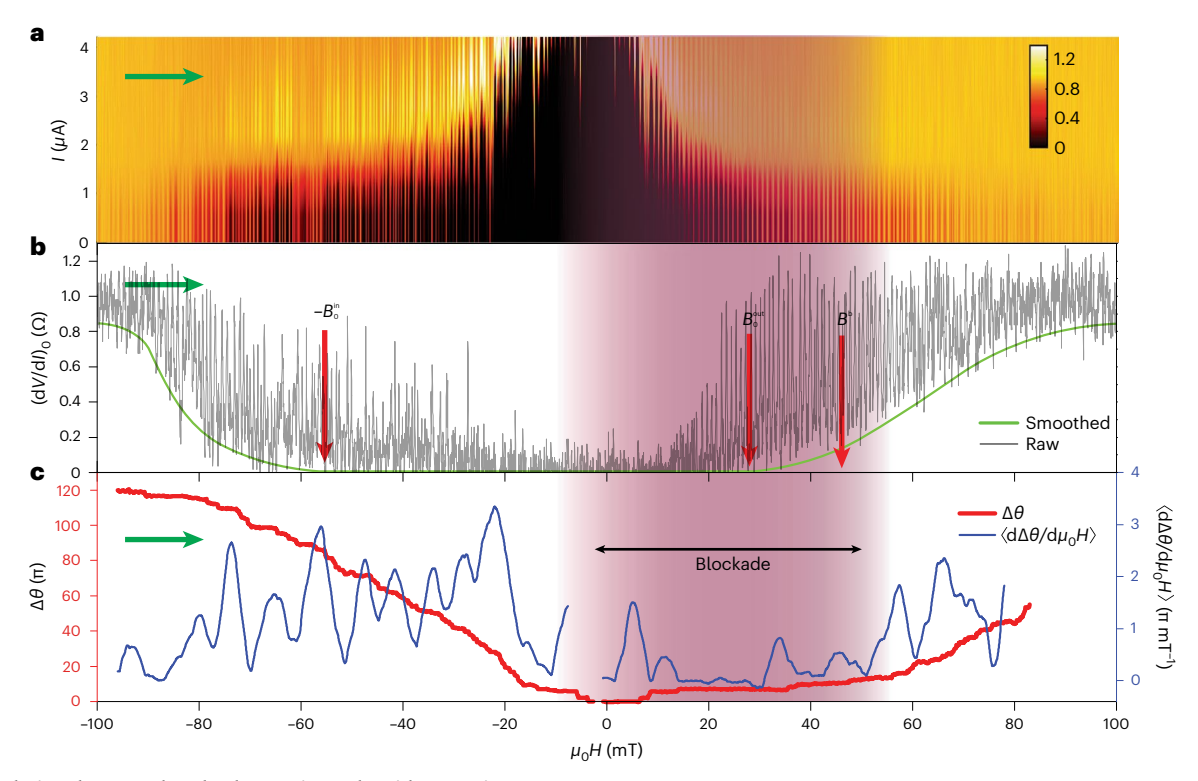


Fig. 5 | Correlating the central peak, phase noise and anti-hysteresis measured in device SA as $\mu_0 H$ is swept from –100 to +100 mT at 18 mK. a, Colour map of dV/dI, highlighting the low-I region. b, The oscillations in the zero-bias $(dV/dI)_0$ (grey curve) together with its floor value (thick green curve). The dissipationless interval for $(dV/dI)_0$ lies between $-B_0^{\rm in} = -54$ mT and

 $B_0^{\rm out}=28\,{\rm mT}$ (red arrows). **c**, The phase noise measured by $\Delta\theta$ (red curve) and $\langle {\rm d}\Delta\theta/{\rm d}\mu_0H\rangle$ (blue curve). Within the quiet zone extending to B^{\flat} on the outbound branch (shaded lilac), the phase noise is suppressed. We infer the existence of a blockade mechanism in this interval. The green arrow in ${\bf a}-{\bf c}$ indicates the field scan direction.

Correlating central peak, phase noise and anti-hysteresis

The phase noise of the edge oscillations provides a window on the behaviour of $\hat{\Psi}(\mathbf{r})$. When pairing in the edge states is compatible with that in the bulk, the oscillations are nearly noise free, whereas incompatibility generates substantial phase noise. The incompatibility strongly affects the phase noise.

Combining the group I and II features with the phase noise measured by $\Delta\theta$ and $\langle d\Delta\theta/d\mu_0H\rangle$ in device SA, we arrive at a consistent picture of the anti-hysteretic behaviour. The colour map of dV/dI and the trace of $(dV/dI)_0$ at 18 mK are displayed in Fig. 5a and 5b, respectively. Starting at –100 mT, the phase noise is initially small, as seen in $\langle d\Delta\theta/d\mu_0H\rangle$ (Fig. 5c, blue curve). This implies that edge pairing is dictated by the Nb amplitude while all pairing of bulk states is suppressed. When H reaches –80 mT, we observe a surge onset in phase noise, which we take as evidence for incompatibility with the vortex liquid that appears in the bulk at –80 mT. The phase noise remains large over the entire interval (–80, –12) mT (Fig. 5c, red curve).

When $\mu_0 H$ crosses -5 mT, $\hat{\Psi}(\mathbf{r})$ switches to s-wave in the bulk as noted above (|H| becomes too weak to de-pair the bulk s-wave condensate). Experimentally, vortices in s-wave superconductors form solids that resist melting throughout the bulk. Consequently, we see a large bulk supercurrent in the field interval (-4, -2) mT identified as the central peak (Fig. 5a), but this favourable interval is brief. When $\mu_0 H$ reaches -2 mT, solidification of the intrinsic vortex liquid causes $\hat{\Psi}(\mathbf{r})$ to revert to the $F_{\alpha\beta}$ symmetry. Suppression of all s-wave paired regions throughout the crystal collapses the central peak before H reaches 0^- . Hence, the placement of the central peak is anti-hysteretic, as observed.

Blockade

When the field crosses zero to the outbound branch (H > 0), we should expect to see the re-appearance of the central peak in the interval (2,4) mT. However, this is not observed in any of the eight devices studied.

The absence of the central peak for H > 0 and the noise suppression in the quiet zone (5, 45) mT suggest a blockade mechanism. Once $\hat{\Psi}$ switches to the intrinsic symmetry $F_{\alpha\beta}$ in the limit $H \to 0^-$, a mechanism appears to block $\hat{\Psi}$ from switching back to s-wave throughout the quiet zone, which extends to a field that we call $B^{\flat} \approx 45$ mT (Fig. 5a–c, shaded lilac). In the quiet zone, pairing in both the edge and bulk states has the $F_{\alpha\beta}$ symmetry. We return to this point below.

The identification of $(dV/dI)_0$ with supercurrents at the edge clarifies considerably the anti-hysteretic loops seen in Fig. 4e,f. As shown by the green curve in Fig. 5b, the dissipationless interval for the edge current spans the interval $(-B_0^{\rm in}, B_0^{\rm out}) = (-54, 28)$ mT for a field scan from left to right. The interval $(-B_0^{\rm in}, B_0^{\rm out})$ is shifted left because, on the inbound branch, edge state pairing follows the s-wave symmetry, whereas on the outbound branch, it adopts the weaker $F_{\alpha\beta}$ pairing. Likewise, in a scan from right to left, $(-B_0^{\rm out}, B_0^{\rm in})$ is shifted right. This accounts for the anti-hysteretic sign of the loops in $(dV/dI)_0$.

Raising the temperature

Figure 6a shows the blockade region (shaded maroon) inferred from field scans from left to right taken at elevated temperatures of 378, 532 and 722 mK (see Fig. 6b for the opposite field scan). The corresponding colour maps of dV/dI are displayed in Fig. 6c–e. For the results at 522 mK, we also show the trace of $(dV/dI)_0$ in Fig. 6f and the phase noise measured by $\Delta\theta$ and $(d\Delta\theta/d\mu_0H)$ (Fig. 6g). The overall patterns are similar to those taken at 18 mK (Fig. 5) except that raising T decreases the field scales. The asymmetry of the phase noise, including its suppression in the blockade interval, is apparent in Fig. 6f,g. We find that the widths of the anti-hysteretic loops in $(dV/dI)_0$, the edge dissipationless interval $(-B_0^{\rm in}, B_0^{\rm out})$ and $B^{\rm b}$ all decrease systematically as T increases, reaching zero at the device $T_{\rm c}$ of approximately 850 mK. The linear decrease of $B^{\rm b}(T)$ as $T \rightarrow T_{\rm c}$ is shown in Supplementary Fig. S9. These trends are

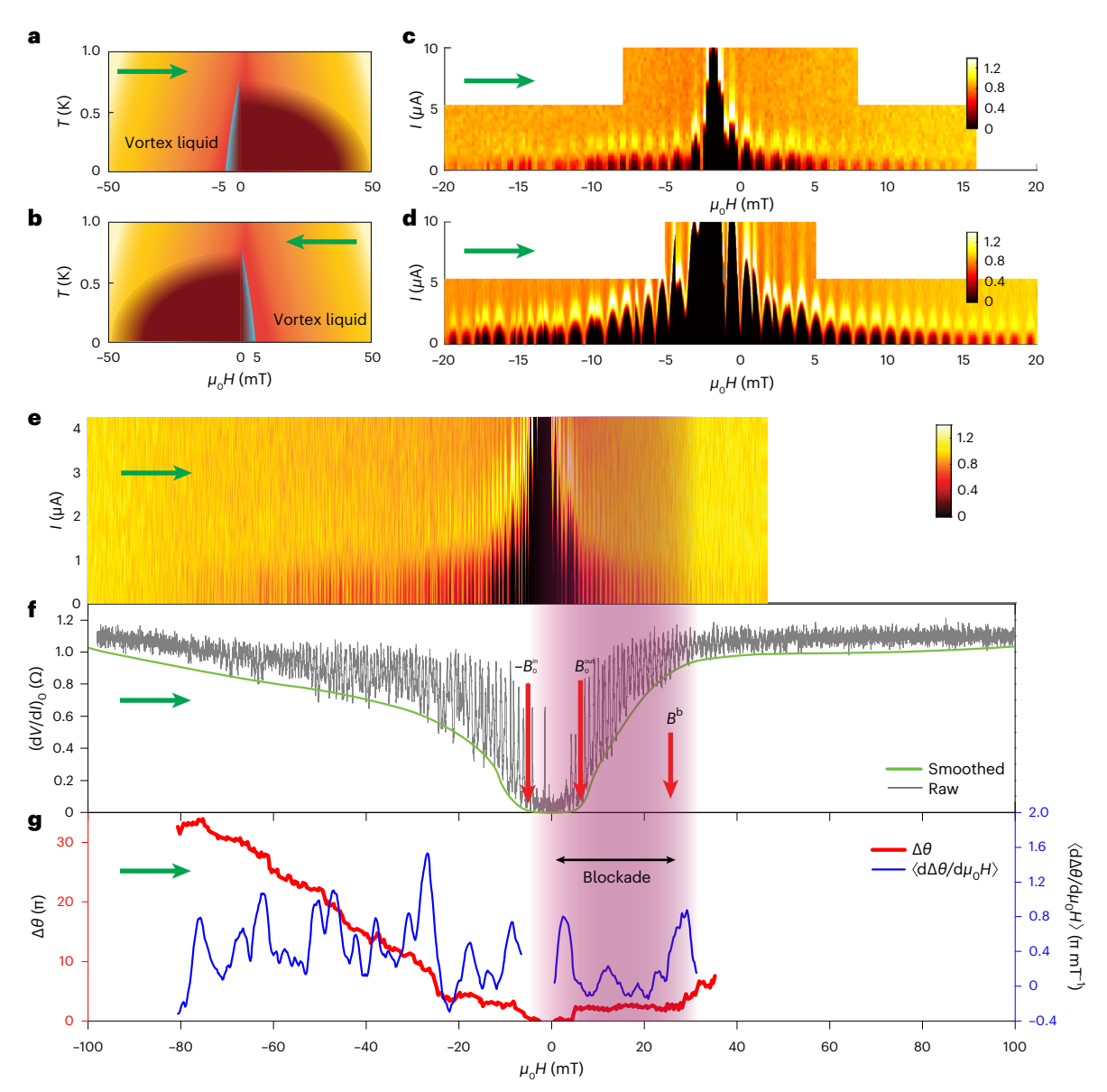


Fig. 6 | **Colour maps, zero-bias** (dV/dI)₀ and phase noise at elevated temperatures in device SA. a,b, The inferred metastable states in the H-T plane for field scans from left to right (a) and right to left (b). The regions where the blockade mechanism operates are shaded maroon. Thin blue stripes indicate regions in which the central peak emerges (note the anti-hysteretic placement). On the outbound branch in a, the maroon region extends to B^{b} (approximately 45 mT) at 18 mK. The dissipative vortex liquid (orange and yellow regions) extend

to ± 80 mT. The device T_c is 850 mK. \mathbf{c} – \mathbf{e} , Colour maps of $\mathrm{d}V/\mathrm{d}I$ measured at 722 mK (\mathbf{c}), 378 mK (\mathbf{d}) and 532 mK (\mathbf{e}). \mathbf{f} , The oscillations in the zero-bias ($\mathrm{d}V/\mathrm{d}I$)₀ (grey curve) and its floor value (green curve). \mathbf{g} , The phase noise measured by $\Delta\theta$ (red curve) and $\langle \mathrm{d}\Delta\theta/\mathrm{d}\mu_0H\rangle$ (blue). The lilac regions in \mathbf{f} and \mathbf{g} represent the quiet zone in which phase noise is minimal. As $T \rightarrow T_c$, the three field scales B_0^{in} , B_0^{out} and B^b all decrease to zero. Green arrows in \mathbf{a} – \mathbf{g} indicate the field scan direction.

consistent with the key role played by $F_{\alpha\beta}$ in generating the anti-hysteresis, phase noise and the blockade.

Hysteretic solid-to-liquid transition

The vortex solid-to-liquid transition is first order, as shown by experiments on cuprates $^{14-17}$. The implied hysteresis suggests a way to understand the blockade mechanism (Fig. 6a,b, maroon region). We conjecture that the blockade mechanism and quiet zone are features intrinsic to the vortex solid. If H is swept from left to right (Fig. 6a), the liquid-to-solid transition is delayed on the inbound branch until $\mu_0 H$ reaches -2 mT, analogous to supercooling of a liquid (regarding |H| as an effective temperature). On the outbound branch, the solid-to-liquid transition is also delayed and shifted to 45 mT. Hence, the observed vortex solid phase is displaced to the right (Fig. 6a). For the opposite

scan, the shift is to the left. We note that the supercooling hysteresis has the conventional sign. However, the blockade mechanism and incompatibility between condensates together displace the bulk and edge supercurrent responses in the opposite direction, which leads to the anti-hystereses in the central peak and $(dV/dI)_0$. Although conjectural at this stage, this supercooling proposal can be subject to tests.

Online content

Any methods, additional references, Nature Portfolio reporting summaries, source data, extended data, supplementary information, acknowledgements, peer review information; details of author contributions and competing interests; and statements of data and code availability are available at https://doi.org/10.1038/s41567-023-02316-9.

References

- Fu, L. & Kane, C. L. Superconducting proximity effect and Majorana fermions at the surface of a topological insulator. *Phys. Rev. Lett.* 100, 096407 (2008).
- 2. Qi, X.-L., Hughes, T. L., Raghu, S. & Zhang, S.-C. Time reversal invariant topological superconductors and superfluids in two and three dimensions. *Phys. Rev. Lett.* **102**, 187001 (2009).
- Fu, L. & Berg, E. Odd-parity topological superconductors: theory and application to Cu_xBi_ySe₃. Phys. Rev. Lett. 105, 097001 (2010).
- Peng, Y., Pientka, F., Berg, E., Oreg, Y. & von Oppen, F. Signatures of topological Josephson junctions. *Phys. Rev. B* 94, 085409 (2016).
- Wang, W. et al. Evidence for an edge supercurrent in the Weyl superconductor MoTe₃. Science 368, 534–537 (2020).
- de Gennes, P. G. Boundary effects in superconductors. Rev. Mod. Phys. 36, 225–237 (1964).
- 7. de Gennes, P. G. Superconductivity of Metals and Alloys (Addison Wesley, 1989).
- Deutscher, G. & de Gennes, P. G. Proximity effects. In Superconductivity, Vol. II (ed. Parks, R. D.) (Taylor and Francis, 1969).
- Ashauer, B., Kieselmann, G. & Rainer, D. On the proximity effect in unconventional superconductors. J. Low Temp. Phys. 63, 349–366 (1986).
- Millis, A., Rainer, D. & Sauls, J. A. Quasiclassical theory of superconductivity near magnetically active interfaces. *Phys. Rev.* B 38, 4504 (1988).
- Sigrist, M. & Ueda, K. Phenomenological theory of unconventional superconductivity. Rev. Mod. Phys. 63, 239–311 (1991).

- Murani, A. et al. Ballistic edge states in Bismuth nanowires revealed by SQUID interferometry. Nat. Commun. 8, 15941 (2017).
- Wang, Y. et al. Anisotropic proximity-induced superconductivity and edge supercurrent in Kagome metal, K1-xV3Sb5. Sci. Adv. 9, eadα726 (2023).
- Safar, H. et al. Experimental evidence for a multicritical point in the magnetic phase diagram for the mixed state of clean, untwinned YBa₂Cu₃O₇. Phys. Rev. Lett. 70, 3800 (1993).
- Zeldov, E. et al. Thermodynamic observation of first-order vortex-lattice melting transition in Bi₂Sr₂CaCu₂O₈. Nature 375, 373–376 (1995).
- Welp, U., Fendrich, J. A., Kwok, W. K., Crabtree, G. W. & Veal, B. W. Thermodynamic evidence for a flux line lattice melting transition in YBa₂Cu₂O₇₋₈, Phys. Rev. Lett. 76, 4809 (1996).
- Soibel, A. et al. Imaging the vortex-lattice melting process in the presence of disorder. *Nature* 406, 282–287 (2000).

Publisher's note Springer Nature remains neutral with regard to jurisdictional claims in published maps and institutional affiliations.

Springer Nature or its licensor (e.g. a society or other partner) holds exclusive rights to this article under a publishing agreement with the author(s) or other rightsholder(s); author self-archiving of the accepted manuscript version of this article is solely governed by the terms of such publishing agreement and applicable law.

© The Author(s), under exclusive licence to Springer Nature Limited 2024

Methods

Device fabrication

The MoTe₂ devices were fabricated following standard nanofabrication procedures. Substrates with pre-patterned alignment makers were prepared in advance. The alignment markers were made of 5 nm of Ti and 50 nm of Au. MoTe₂ microflakes were mechanically exfoliated onto the substrates using Nitto Denko SPV 5057A5 surface protection tape. Microflakes with adequate sizes and sharp edges were chosen using an optical microscope.

Niobium electrodes were made following the standard polymethyl methacrylate-copolymer bilayer recipe. After the resists were spun on top of substrates, contacts were patterned using an EBPG 5150 (Raith). The devices were developed with methyl isobutyl ketone:isopropyl alcohol (1:3) solution for 60 s and rinsed with isopropyl alcohol solution. The devices were then transferred to an EvoVac sputtering system (Angstrom Engineering). An in situ Ar plasma beam was applied to the surfaces of the devices for 120 s to remove the top few layers of MoTe $_2$ that were oxidized. A thin (3 nm) layer of Ti layer was sputtered at a rate of 0.1– $0.2\,\mathrm{nm}\,\mathrm{s}^{-1}$ to form a sticking layer, followed by 100 nm of Nb deposited at a rate of 1 nm s $^{-1}$. Finally, 5 nm of Au was sputtered on top of the Nb layer to protect it from oxidization. All sputtering procedures were performed at high vacuum of approximately 10^{-8} mbar.

Measurement techniques

Measurements were carried out in a top-loading dilution refrigerator (KelvinoxTLM; Oxford Instruments). Once loaded into the fridge, devices were immersed in the circulating ${}^3\text{He}^{-4}\text{He}$ mixture in the mixing chamber. The base temperature of the fridge was $T \approx 20$ mK. Three filters were used to reduce noise during measurements. An LC π filter, located at the top of the probe, provided 80 dB suppression for frequencies f > 100 MHz. The two other filters were located in the mixing chamber. The first one was a sintered metal powder filter consisting of Cu particles of 30-60 μ m in diameter. It suppressed any stray electromagnetic radiation for frequencies f > 1 GHz. The second filter was a low-pass RC filter with a cutoff frequency of f = 300 kHz. An NbTi superconducting magnet was used to apply magnetic fields to devices. A Keithley 2400 and a Keithley 6221 provided the current to the superconducting magnet. The smallest field step size was as small as a few microteslas.

Differential resistances of all devices were measured using a SR830 lock-in amplifier. A d.c. bias from a Keithley 2400 voltage source was superposed with a small a.c. excitation voltage from the lock-in amplifier through a home-made voltage adder. The resulting voltage was converted to current through a buffer resistor that was orders of magnitude larger in resistance than the device of interest. The voltage signal V across the device was first passed through a pre-amplifier to improve the signal-to-noise ratio. The gain was usually $G \approx 1,000$. The amplified signal then reached the lock-in amplifier for detection. Measurements were done in quasi-four-point fashion. Although both voltage and current contacts shared the same electrodes, the electrodes were superconducting at 20 mK.

The differential resistance plots in the main text were obtained through the following procedures: First, the magnetic field was set

to the desired value. Then, the d.c. bias was ramped from zero to the desired bias value with a small step size. After reaching the desired bias, the current was ramped back to zero with a much larger step size. Such procedures were repeated for desired field ranges. The collected differential resistance curves were plotted together. The differential resistance versus field at zero bias $(dV/dI)_0$ plots were prepared as follows: Starting with the field at zero, we swept H to its maximum negative value then to the maximum positive value before returning to zero.

Data availability

The data presented in this work are available in a figshare repository¹⁸. Source data are provided with the paper. Any additional data are available from the corresponding author upon request.

References

 Kim, S., Lei, S., Schoop, L. M., Cava, R. J. & Ong, N. P. Edge supercurrent reveals competition between condensates in a Weyl superconductor. Data sets. figshare https://doi.org/10.6084/ m9.figshare.22635019 (2023).

Acknowledgements

We benefitted from discussions with W. Wang and Z. Zhu. N.P.O. and S.K. were supported by the United States Department of Energy (DE-SC0017863). The crystal growth effort was supported by an MRSEC grant from the United States National Science Foundation (NSF DMR-2011750) that supported S.L., L.M.S., R.J.C. and N.P.O. The Gordon and Betty Moore Foundation's EPiQS initiative provided generous support via grants GBMF9466 (N.P.O.) and GBMF9064 (L.M.S.).

Author contributions

S.K. and N.P.O. conceptualized and designed the experiment. S.K. performed all device fabrication and measurements. The crystals were grown by S.L., L.M.S. and R.J.C. Analysis of the data was carried out by S.K. and N.P.O., who jointly wrote the manuscript.

Competing interests

The authors declare no competing interests.

Additional information

Supplementary information The online version contains supplementary material available at https://doi.org/10.1038/s41567-023-02316-9.

Correspondence and requests for materials should be addressed to N. P. Ong.

Peer review information *Nature Physics* thanks Guangtong Liu and the other, anonymous, reviewer(s) for their contribution to the peer review of this work.

Reprints and permissions information is available at www.nature.com/reprints.